Materials Transactions, Vol. 49, No. 6 (2008) pp. 1284 to 1293
©2008 The Japan Institute of Metals

Dynamic Deformation Behaviour and Microstructural Evolution of High-Strength Weldable Aluminum Scandium (Al-Sc) Alloy

Woei-Shyan Lee*[1] and Tao-Hsing Chen*[2]

Department of Mechanical Engineering, National Cheng Kung University, Tainan 701, Taiwan, R.O.China

A compressive split-Hopkinson pressure bar is used to investigate the dynamic deformation behaviour, fracture characteristics and microstructural evolution of high-strength weldable aluminum scandium (Al-Sc) alloy at strain rates ranging from $1.3 \times 10^3\ s^{-1}$ to $5.9 \times 10^3\ s^{-1}$ under room temperature conditions. The stress-strain curves reveal that the dynamic mechanical behaviour response of the Al-Sc alloy is highly sensitive to both the strain and the strain rate. As the strain rate increases, the flow stress, work hardening rate and strain rate sensitivity all increase, but the fracture strain and activation volume decrease. The Zerilli-Armstrong FCC constitutive model is applied to describe the high strain rate plastic behaviour of the Al-Sc alloy. A good agreement is found between the predicted flow response and the actual response at all values of the applied strain rate. The Al-Sc alloy specimens fracture primarily as a result of a localised shearing effect. Scanning electron microscopy observations indicate that the fracture features are characterised by a transgranular dimple-like structure. The density and depth of the dimples decrease with increasing strain rate. Transmission electron microscopy observations reveal the presence of Al_3Sc particles in the matrix and at the grain boundaries. These particles prevent dislocation motion and therefore prompt a significant strengthening effect. The microstructural observations also reveal that the dislocation density and degree of dislocation tangling increase with increasing strain rate. The variations observed in the dislocation cell structure reflect differing degrees of strain rate sensitivity and activation volume and are found to be consistent with the observed stress-strain response of the Al-Sc alloy. [doi:10.2320/matertrans.MRA2008032]

(Received January 25, 2008; Accepted March 13, 2008; Published May 1, 2008)

Keywords: *aluminum-scandium alloy, strain rate effect, strain rate sensitivity, activation volume, localised shearing, dislocation*

1. Introduction

High-strength weldable aluminum alloy has many applications within the aerospace and automotive industries. The strength of aluminum alloy is traditionally enhanced via the addition of small quantities of zirconium (Zr), manganese (Mn) and chromium (Cr). However, it has recently been shown that the addition of scandium (Sc) yields a remarkable improvement in both the mechanical properties and the weldability of aluminum alloys as a result of a grain refinement effect, a modification of the cast microstructure, an improved resistance to recrystallisation and a reduction in the hot-cracking property of the alloy.[1)] The strengthening effect yielded by the addition of Sc is a result primarily of the formation of fine, highly-dispersed Al_3Sc precipitates within the Al matrix. The precipitates induce a strain mismatch effect which suppresses the movement of dislocations and inhibits recrystallisation. As a result of its many favorable mechanical properties, weldable Al-Sc alloy has received significant attention in recent years and has been utilised for many diverse applications ranging from sports equipment, to missile and aviation components, automotive products, and so forth.

Structural engineering components are invariably exposed to many forms of high strain rate loading during their manufacture or subsequent service lives. To predict the dynamic response of these components, it is therefore necessary to develop a detailed knowledge of their mechanical properties and microstructural characteristics under representative strain rate conditions. However, while the literature contains numerous investigations into various aspects of Al-Sc alloy, *e.g.* its resistance to recrystallisation,[2–4)] its work hardening[5–7)] and superplastic[8–10)] properties, and its enhanced weldability characteristics,[11–14)] its high strain rate behaviour has attracted relatively little attention. Accordingly, the current study uses a compressive split-Hopkinson pressure bar (SHPB) to examine the dynamic deformation behaviour, fracture characteristics and microstructural evolution of high-strength weldable Al-Sc alloy at strain rates ranging from $1.3 \times 10^3\ s^{-1}$ to $5.9 \times 10^3\ s^{-1}$ under room temperature conditions. The stress-strain relations of the Al-Sc alloy are obtained at each value of the strain rate and a constitutive equation is developed to predict the flow response of the alloy. The fracture surfaces are examined using a scanning electron microscopy (SEM) technique in order to identify the dominant fracture mechanism. Finally, transmission electron microscopy (TEM) observations are performed to characterise the microstructures of the fractured specimens under various strain rate conditions.

2. Material and Experimental Procedure

The Al-Sc alloy used in the current study was supplied by Taiwan Hodaka Technology Co., Ltd. and had a mass% chemical composition of 6.8% Zn, 2.2% Mg, 0.15% Zr, 0.13% Sc, and a balance of Al. The alloy was melted in a pit type electrical resistance furnace at a temperature of 700°C and was then poured into a heated permanent metal mould measuring 55 mm × 170 mm (diameter × length). The cast ingot was homogenised at 480°C for 16 h and was then transferred to a preheated extrusion mold. After holding at 500°C for 2 h, the ingot was extruded using an indirect extrusion machine to form a bar with dimensions of 15 mm × 650 mm (diameter × length). To ensure an optimum precipitation and distribution of the Al_3Sc particles within the matrix, the extruded bar was solution heat-treated in an air

*[1]Corresponding author, E-mail: wslee@mail.ncku.edu.tw
*[2]Graduate Student, National Cheng Kung University

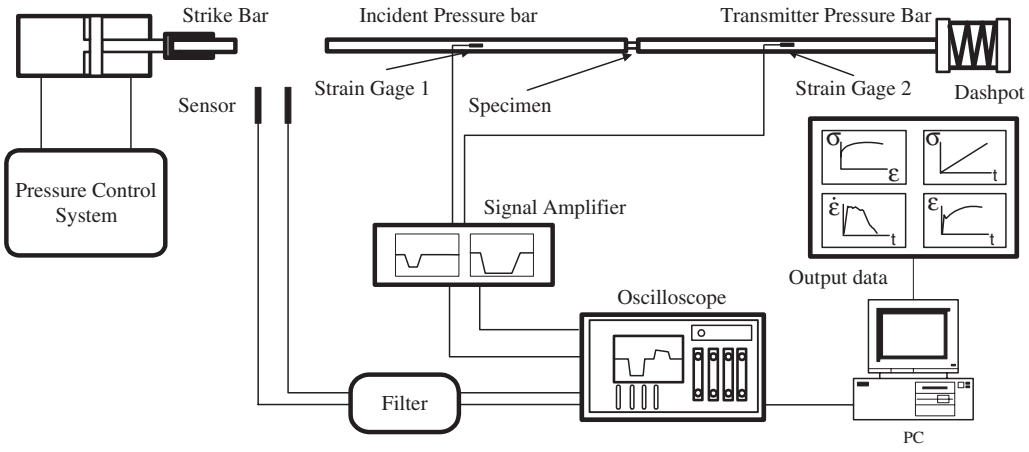

Fig. 1 Schematic illustration of compressive split-Hopkinson bar apparatus.

furnace at 465°C for 1 h, water quenched at room temperature, and then aged naturally for 3 days. Finally, the bar was processed using a two-step artificial aging treatment procedure performed at 105°C for 7 h followed by 150°C for 10 h, respectively.

Following the aging process, specimens with a length of 7 ± 0.1 mm and a diameter of 7.2 mm were machined from the bar and finished to a final diameter of 7 ± 0.1 mm using a centre-grinding process. Compressive deformation experiments were then conducted at room temperature under both quasi-static and dynamic strain rates. The quasi-static properties of the Al-Sc alloy were evaluated using an MTS 810 material testing system (MTS Systems, USA) at a nominal strain rate of $10^{-3}\,s^{-1}$. A series of dynamic impact tests was then performed at room temperature using a compressive SHPB system at strain rates between $1.3 \times 10^3\,s^{-1}$ and $5.9 \times 10^3\,s^{-1}$. As shown schematically in Fig. 1, the SHPB system consisted of a striker bar, an incident pressure bar and a transmitted pressure bar. The striker bar was manufactured of high-strength tool steel and had a diameter of 12.7 mm and a length of 368 mm. Furthermore, the incident pressure bar and the transmitted pressure bar were made of high-strength tool steel and measured 12.7 mm × 100 cm (diameter × length). In the impact test, the cylindrical specimen was sandwiched between the incident pressure bar and the transmitted bar and the end of the incident bar was then impacted by the strike bar.

The impact of the strike bar on the incident pressure bar generates a compressive wave which propagates along the incident bar toward the specimen. Upon reaching the interface between the incident pressure bar and the specimen, part of the wave is reflected back along the incident bar, while the remainder is transmitted through the specimen. The amplitudes of the incident, reflected and transmitted pressure pulses, denoted by ε_i, ε_r and ε_t, respectively, are recorded by strain gauges mounted on the incident and transmitted bars. In accordance with one-dimensional elastic wave propagation theory, the compressive strain ε, the strain rate $\dot{\varepsilon}$ and the flow stress σ are given respectively by

$$\varepsilon = -\frac{2C_0}{L}\int \varepsilon_r dt, \tag{1}$$

$$\dot{\varepsilon} = -\frac{2C_0}{L}\varepsilon_r, \tag{2}$$

$$\sigma = \frac{EA}{A_s}\varepsilon_t, \tag{3}$$

where E and C_0 are the Young's modulus of the steel bars and the elastic wave velocity, respectively, L is the initial specimen length, and A and A_s are the cross-sectional areas of the bars and the specimen, respectively. Following each experiment, the values of the stress and strain recorded continuously over the duration of the impact test were plotted against one another to produce the corresponding dynamic stress-strain curve. It was found that the curves produced at each value of the strain rate exhibited marked oscillations as a result of the dispersion of the elastic compressive wave as it propagates along the pressure bars. Accordingly, a discrete Fourier transformation process was performed to correct each curve. Figure 2 presents the original and modified stress-strain curves for the particular case of a specimen deformed at a strain rate of $3.6 \times 10^3\,s^{-1}$.

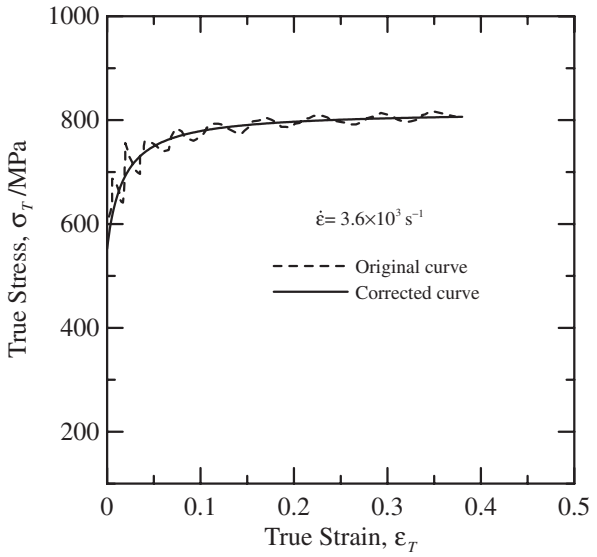

Fig. 2 Original and corrected stress-strain curves for Al-Sc alloy deformed at strain rate of $3.6 \times 10^3\,s^{-1}$ at room temperature.

Following the impact tests, fracture specimens were prepared using a standard metallographic method. The specimens were examined using a Philip's XL-40FEG SEM with a scanning voltage of 15 kV to identify the dominant fracture mechanism. Thereafter, specimens for TEM microstructural observations were prepared by cutting foils with a thickness of 350 μm from the deformed specimens using a low speed cutting machine. Disks with a diameter of 3 mm were punched from each foil, mechanically ground to a thickness of around 200 μm using 1200 grit paper and then electro-polished in a solution of 30% nitric acid and 70% methanol at a temperature of −30°C using a Struers Tenupol twin-jet polishing system with an agitation voltage of 15 V. The microstructural characteristics of the various specimens were then examined using a JEOL TEM-3010 transmission electron microscope with a scanning voltage of 200 kV.

3. Results and Discussion

3.1 True stress-strain curves

Figure 3(a) illustrates the true stress-strain curves obtained for the weldable Al-Sc alloy at a nominal strain rate of $10^{-3}\,s^{-1}$ and at strain rates ranging from $1.3 \times 10^3\,s^{-1}$ to $5.9 \times 10^3\,s^{-1}$. It is evident that the flow stress of the Al-Sc alloy is sensitive to both the strain rate and the strain. It can be seen that for a constant strain rate, the flow stress increases gradually with increasing strain, while for a constant strain, the flow stress increases rapidly with increasing strain rate. From inspection, it is determined that for a constant true strain of 0.5, the flow stress increases by approximately 250 MPa as the strain rate is increased from a quasi-static rate of $10^{-3}\,s^{-1}$ to a dynamic rate of $1.3 \times 10^3\,s^{-1}$. Moreover, it is found that the strain rate governs not only the flow stress, but also the facture strain. Specifically, the fracture strain increases as the strain rate decreases. However, the specimens deformed at strain rates lower than $1.3 \times 10^3\,s^{-1}$ do not fracture, even when deformed to true strains as high as 0.52. Thus, it can be inferred that the weldable Al-Sc alloy has excellent deformability characteristics under high strain rate conditions. Figure 3(b) compares the flow stress-strain curve for an Al-Sc alloy specimen deformed at a strain rate of $1.3 \times 10^3\,s^{-1}$ with the curves presented in the literature for 7075-T6 alloy[15] and 6061-T6 alloy,[16] respectively, under similar strain rate conditions. It can be seen that for any given strain, the stress induced within the Al-Sc alloy is greater than that produced in either of the other two alloys, and thus it can be inferred that the addition of Sc to the Al alloy yields a significant improvement in its mechanical strength.

The stress-strain responses of the Al-Sc alloy shown in Fig. 3(a) can be described by an empirical power law of the form $\sigma = \sigma_y + B\varepsilon^n$, where σ_y is the yield strength, B is a material constant, and n is the work hardening coefficient. Table 1 summarises the values of all three parameters at each of the strain rates considered in the present study. Note that the fracture strain and fracture stress data are also presented for comparison purposes. As expected, the yield strength, material constant and work hardening coefficient all increase with increasing strain rate. In Fig. 3(a), the work hardening rate ($d\sigma/d\varepsilon$) at any value of the strain rate is equivalent to the

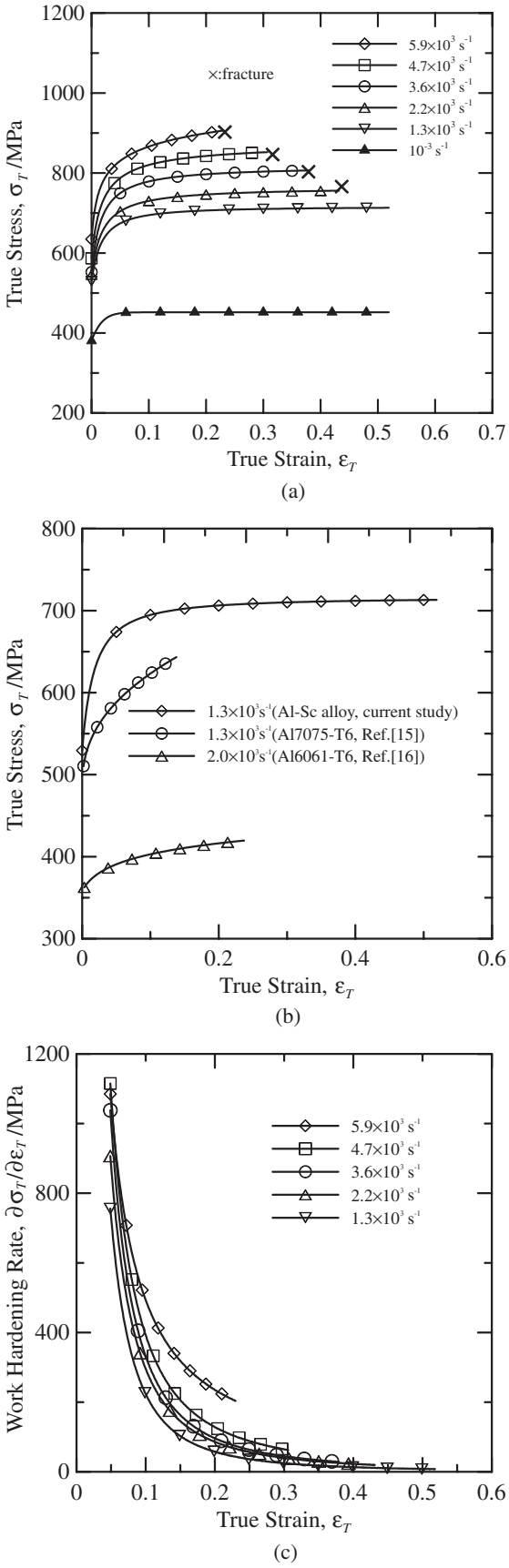

Fig. 3 (a) Stress-strain curves of weldable Al-Sc alloy deformed at various strain rates under room temperature conditions; (b) comparison of stress-strain curve of weldable Al-Sc alloy with those of 7075 T6 alloy and 6061 T6 alloy under similar strain rate conditions; (c) variation of work hardening rate of weldable Al-Sc alloy with strain as function of strain rate.

Table 1 Mechanical properties of weldable Al-Sc alloy deformed under different strain rate conditions.

Strain rate $\dot{\varepsilon}$ (s^{-1})	Yield strength (MPa)	Material constant (MPa)	Work hardening coefficient, n	Fracture strain	Fracture stress (MPa)
1.3×10^3	583.4	153.5	0.17	—	—
2.2×10^3	595.6	198.9	0.18	0.43	755.9
3.6×10^3	606.5	254.2	0.20	0.37	806.4
4.7×10^3	619.4	320.6	0.23	0.3	852.2
5.9×10^3	644.3	412.5	0.28	0.23	906.4

gradient of the corresponding stress-strain curve. Therefore, it is clearly seen that the work hardening rate of the Al-Sc alloy is dependent on both the strain rate and the strain. Figure 3(c) illustrates the variation of the work hardening rate with the true strain as a function of the strain rate. It is observed that for a constant strain, the work hardening rate increases with increasing strain rate. As will be discussed later, this is the consequence of an interaction between the Al_3Sc precipitates in the Al-Sc alloy and the dislocations within the microstructure. Figure 3(c) also shows that for a constant strain rate, the work hardening rate decreases with increasing strain. Again, it will be shown later that this is the result of a lower motion of the dislocations under higher strains.

3.2 Strain rate sensitivity and activation volume

The correlation between the flow stress and the strain rate can be visualised more clearly by plotting the flow stress as a function of the logarithmic strain rate. Figure 4(a) shows the stress-log strain curves at true strain values of 0.05, 0.1 and 0.2, respectively. It can be seen that the flow stress increases dramatically with increasing strain rate and strain. Table 2 summarises the values of the strain rate sensitivity parameter β (where $\beta = (\partial\sigma/\partial \ln \dot{\varepsilon})$ over the quasi-static and dynamic strain rate range considered in the present study. It can be seen that for a constant strain, the strain rate sensitivity increases with increasing strain rate, while for a given strain rate, the strain rate sensitivity increases slightly with increasing strain.

In order to clarify the respective dependencies of the strain rate sensitivity and the activation volume on the microstructural evolution of the Al-Sc alloy under different loading conditions, the two properties can be plotted against the work hardening stress ($\sigma - \sigma_y$), where σ_y is the yield strength. As shown in Fig. 4(a), the flow stress induced within the Al-Sc alloy is highly sensitive to the strain rate, which suggests that the dynamic response of the Al-Sc alloy is dominated by a specific rate-controlling deformation mechanism. Assuming that the strain rate is controlled by a thermally-activated process with a free energy of activation ΔG^*, the relationship between the flow stress and the strain rate can be expressed in the form of the following Arrhenius equation:

$$\dot{\varepsilon} = \dot{\varepsilon}_0 \exp[-\Delta G^*/K_b T], \tag{4}$$

where ε_0 is the frequency factor, ΔG^* is the activation energy, K_b is the Boltzmann constant, and T is the absolute temperature.

The variation of the activation energy with the loading condition is given by[17–19]

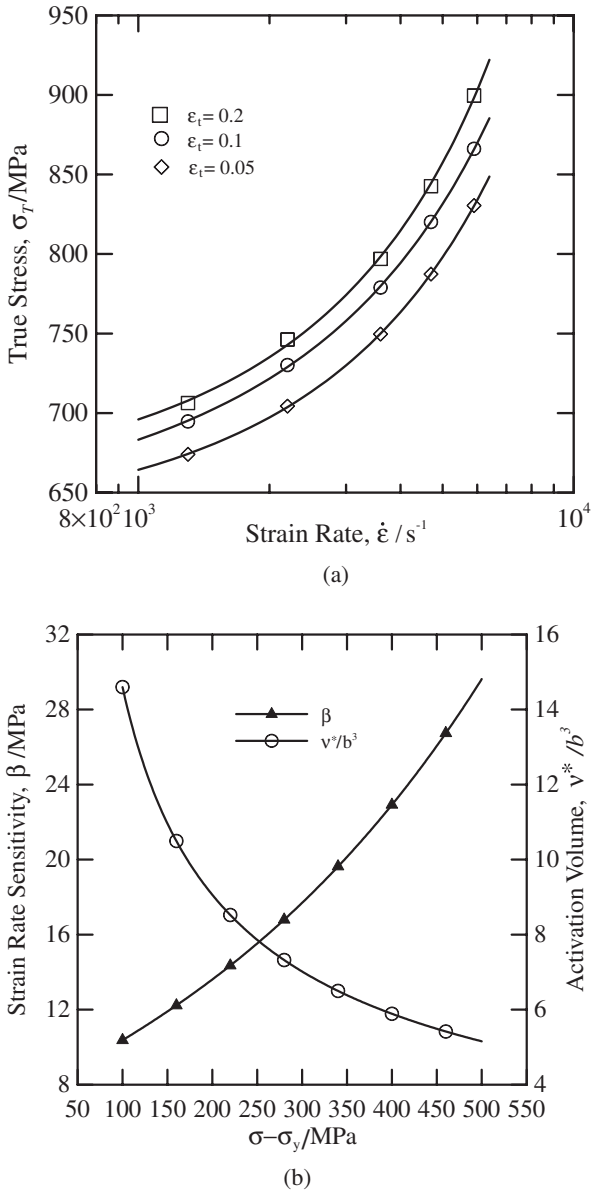

Fig. 4 (a) Variation of flow stress with strain rate as function of plastic strain; (b) variation of strain rate sensitivity and activation volume as function of work hardening stress ($\sigma - \sigma_y$).

$$\Delta G^* = -T\nu^*[\partial\sigma/\partial T]_{\dot{\varepsilon},\varepsilon}, \tag{5}$$

where ν^* is the activation volume and has the form

$$\nu^* = K_b T\left(\frac{\partial \ln \dot{\varepsilon}}{\partial \sigma}\right) = \frac{K_b T}{\beta}. \tag{6}$$

Table 2 Strain rate sensitivity and activation volume of weldable Al-Sc alloy computed over quasi-static and dynamic strain rate range.

True strain ε_t	Static flow stress σ_s (MPa)	Dynamic flow stress σ_d (MPa)	Strain rate sensitivity β (MPa)	Activation Volume v^*/b^3
For $\dot{\varepsilon}_s = 10^{-3}\,s^{-1}$ and $\dot{\varepsilon}_d = 1.3 \times 10^3\,s^{-1}$				
0.1	470.8	694.7	13.9	9.0
0.15	473.2	702.4	14.2	8.9
0.2	474.2	706.3	14.3	8.7
For $\dot{\varepsilon}_s = 10^{-3}\,s^{-1}$ and $\dot{\varepsilon}_d = 2.2 \times 10^3\,s^{-1}$				
0.1	470.8	730.2	15.5	8.4
0.15	473.2	740.6	15.9	8.2
0.2	474.2	746.3	16.3	7.8
For $\dot{\varepsilon}_s = 10^{-3}\,s^{-1}$ and $\dot{\varepsilon}_d = 3.6 \times 10^3\,s^{-1}$				
0.1	470.8	778.9	17.5	7.4
0.15	473.2	790.6	17.8	7.2
0.2	474.2	796.9	18.3	6.9
For $\dot{\varepsilon}_s = 10^{-3}\,s^{-1}$ and $\dot{\varepsilon}_d = 4.7 \times 10^3\,s^{-1}$				
0.1	470.8	820.1	20.1	6.4
0.15	473.2	834.4	20.5	6.3
0.2	474.2	842.6	20.9	6.0
For $\dot{\varepsilon}_s = 10^{-3}\,s^{-1}$ and $\dot{\varepsilon}_d = 5.9 \times 10^3\,s^{-1}$				
0.1	470.8	866.2	24.3	5.5
0.15	473.2	885.9	24.9	5.3
0.2	474.3	899.6	25.3	5.1

Table 2 indicates the activation volume of the Al-Sc alloy under each of the current strain and strain rate conditions. Note that the activation volume data are normalised by b^3, where b is the Burger's vector (equal to 0.286 nm for the present Al-Sc alloy). Figure 4(b) illustrates the variation of the strain rate sensitivity and the normalised activation volume as a function of the work hardening stress. The results show that the strain rate sensitivity increases with increasing work hardening stress. This phenomenon is most likely the result of a more intensive interaction between the Al_3Sc precipitates and the dislocations at higher strain rates and strain, which in turn prompts the formation of additional cell structures. In general engineering materials, a thermal activation effect enables dislocations to overcome obstacles in the microstructure during the plastic deformation process. However, as shown in Fig. 4(b), the activation volume decreases rapidly with increasing work hardening stress, which implies that the dislocations receive only limited assistance in overcoming the obstacles posed by the Al_3Sc precipitates in the matrix and at the grain boundaries.

3.3 Deformation constitutive equation

Constitutive equations provide a convenient means of predicting the behaviour of general engineering materials over a range of dynamic impact loading conditions.[20,21] This study applies the Zerilli-Armstrong FCC constitutive equation,[22,23] which is based on the principles of dislocation-mechanics theory, to predict the dynamic deformation behaviour of the current weldable Al-Sc alloy. This constitutive equation has the form

$$\sigma = \sigma_0 + c_2\varepsilon^n[\exp(-c_3T + c_4T\ln\dot{\varepsilon})], \qquad (7)$$

where σ is the flow stress, ε is the strain, $\dot{\varepsilon}$ is the strain rate, T is the temperature, and σ_0, c_2, c_3, c_4 and n are material constants.

In modeling the dynamic response of the Al-Sc alloy, it is necessary to take account of the temperature rise generated by the plastic deformation process. Therefore, the temperature term (T) in eq. (7) is replaced by $T = T_0 + \Delta T$, where T_0 is the experimental temperature (*i.e.* room temperature in the current case) and ΔT is the temperature rise induced by plastic deformation and is given by $\Delta T = [0.9/\rho C_p]\int_0^{\varepsilon}\sigma d\varepsilon$, where ρ is the density of the Al-Sc alloy (2.78 g/cm^3), C_p is the heat capacity (0.92 J g^{-1} per°C), σ is the flow stress and $d\varepsilon$ is the strain interval. The parameters in the Zerilli Armstrong constitutive equation were derived using SigmaPlot software. In the derivation process, the experimental data in Fig. 5 were substituted into the constitutive equation and an iterative procedure based upon a least squares regression technique was performed to establish the parameter values which yielded the best-fit approximation to the experimental stress-strain curves. The results indicated that the optimal parameter values were as follows: $\sigma_0 =$ 630.2 MPa, $c_2 = 170.8$ MPa, $c_3 = 0.023$ (K^{-1}), $c_4 = 2.34 \times 10^{-3}$ (K^{-1}) and $n = 0.39$. Figure 5 compares the original experimental stress-strain curves (reproduced directly from Fig. 3(a)) with those predicted by the Zerilli-Armstrong equation under equivalent strain rate conditions. It is evident that a good agreement exists between the two sets of results in every case, and thus the suitability of the Zerilli-Armstrong FCC constitutive equation for predicting the dynamic deformation behaviour of Al-Sc alloy under room temperature conditions is confirmed.

3.4 Fracture analysis and fractrographic observations

The fracture mode and fracture surface characteristics of

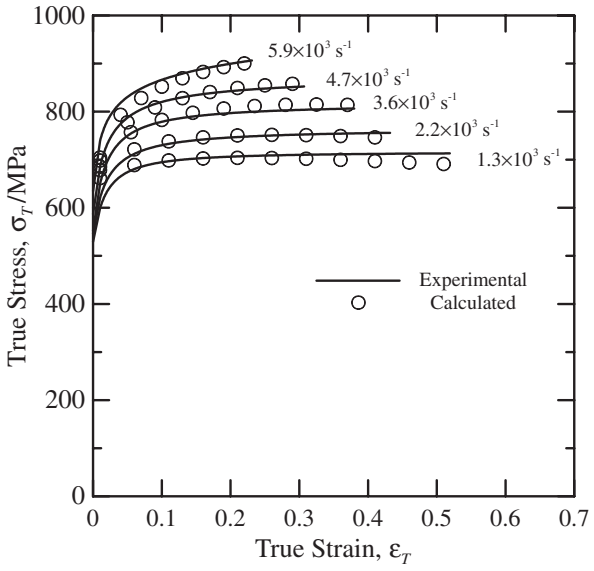

Fig. 5 Comparison of measured and predicted flow stress-strain curves.

Table 3 Stress-strain conditions associated with occurrence of fracture in weldable Al-Sc alloy.

Strain rate (s^{-1})	True strain	Fracture state
1.2×10^3	0.52	○
2.2×10^3	0.43	●
3.2×10^3	0.37	●
4.7×10^3	0.3	●
5.8×10^3	0.23	●

○: safe; ●: fracture by shearing

the Al-Sc specimens were observed using an SEM technique. Figure 6(a) presents a low-magnification SEM fractograph of a specimen deformed at a strain rate of $3.6 \times 10^3\ s^{-1}$. It is observed that the specimen fractures along a plane oriented at around 45° with respect to the loading direction. This plane corresponds to the plane of maximum shear stress, and hence it can be inferred that the specimen fracture is dominated by a localised shearing effect.

Table 3 summarises the stress and strain conditions associated with the occurrence of cracking and fracture in the present Al-Sc specimens. The results show that specimen fracture is dependent not only the strain rate, but also on the plastic strain. Figures 6(b)–6(e) illustrate the fracture features of specimens deformed at strain rates of $2.2 \times 10^3\ s^{-1}$, $3.6 \times 10^3\ s^{-1}$, $4.7 \times 10^3\ s^{-1}$ and $5.9 \times 10^3\ s^{-1}$, respectively. In the fractograph presented in Fig. 6(b), it can be seen that the fracture surface is characterised by a transgranular dimple-like structure, which is indicative of a ductile fracture mode. Moreover, it is observed that the dimples are elongated along the shear direction. In the specimen impacted at a higher strain rate of $3.6 \times 10^3\ s^{-1}$, the fracture surface is still dominated by a dimple-like structure (see Fig. 6(c)), but the dimple features are shallower and more sparsely dispersed. When the strain rate is increased to $4.7 \times 10^3\ s^{-1}$ and $5.9 \times 10^3\ s^{-1}$ respectively, a further reduction is observed in both the dimple depth and the dimple density (see Figs. 6(d) and 6(e), respectively). Moreover, it is apparent that the higher strain rate induces a greater number of flat cleavage planes in the fracture surface. This suggests that an increased strain rate reduces both the ductility of the specimen and its fracture resistance. This result is consistent with the experimental stress-strain curves presented in Fig. 3, which show that the fracture strain decreases with an increasing strain rate.

3.5 Microstructural evolution

To further investigate the effect of the strain rate on the microstructural evolution of the current weldable Al-Sc alloy, the microstructures of various deformed and undeformed specimens were observed using a TEM technique. Figure 7(a) shows the microstructure of an undeformed specimen and reveals the presence of a random distribution of fine and coarse precipitates within the matrix and aligned along the grain boundaries. The results of an energy dispersive spectroscopy (EDS) analysis reveal these precipitates to be Al_3Sc phases. A close inspection of the TEM image shows that the microstructure of the undeformed specimen also contains a small number of dislocations. Figure 7(b) illustrates the microstructure of an Al-Sc specimen deformed at a strain rate of $1.3 \times 10^3\ s^{-1}$. In this case, the substructure consists of an arrangement of loosely-tangled dislocation cells. The greater number of dislocations in the microstructure of the deformed specimen is most likely the result of a barrier effect caused by the presence of Al_3Sc precipitates in the matrix and grain boundary, which prevents the dislocations from moving and thus results in their generation and accumulation instead. Note that the formation of dislocation cells in the current Al-Sc specimens under high strain rate loading conditions is consistent with the high stacking fault energy effect identified in,[24] in which it was reported that materials with a high stacking fault energy (such as Al-Sc) are prone to cross-slip and cell formation effects under high strain rate loading. When the strain rate is further increased to $3.6 \times 10^3\ s^{-1}$, Fig. 7(c) shows that the microstructure contains a large number of small, well-defined dislocation cells with thin walls. From inspection, it can be seen that the higher strain rate induces a particularly high dislocation density around the Al_3Sc particles, which again confirms the barrier effect imposed by the Al_3Sc phases on the dislocation motion. Figure 7(d) presents the dislocation structure of an Al-Sc specimen deformed at a strain rate of $5.9 \times 10^3\ s^{-1}$. In this case, the dislocation cell structure has a very well-developed form and the cell walls comprise a dense arrangement of tangled dislocations. Comparing Fig. 7(d) with Fig. 7(c), it is evident that the size of the dislocation cells and the thickness of the cell walls both reduce as the strain rate increases. Overall, the TEM images shown in Figs. 7(b)–7(d) indicate that the increased flow stress and work hardening rate observed at higher strain rates in Fig. 3(a) can be attributed to a refinement of the dislocation cell structure as the strain rate is increased.

The microstructural properties of the various deformed specimens were further evaluated in terms of the cell size, the ratio of the dislocation cell size to the cell wall thickness and the dislocation density, *i.e.* $\rho = 2n/Lt$,[25] where n is the number of intersections between a dislocation and a random set of lines of length L and t is the foil thickness. The values

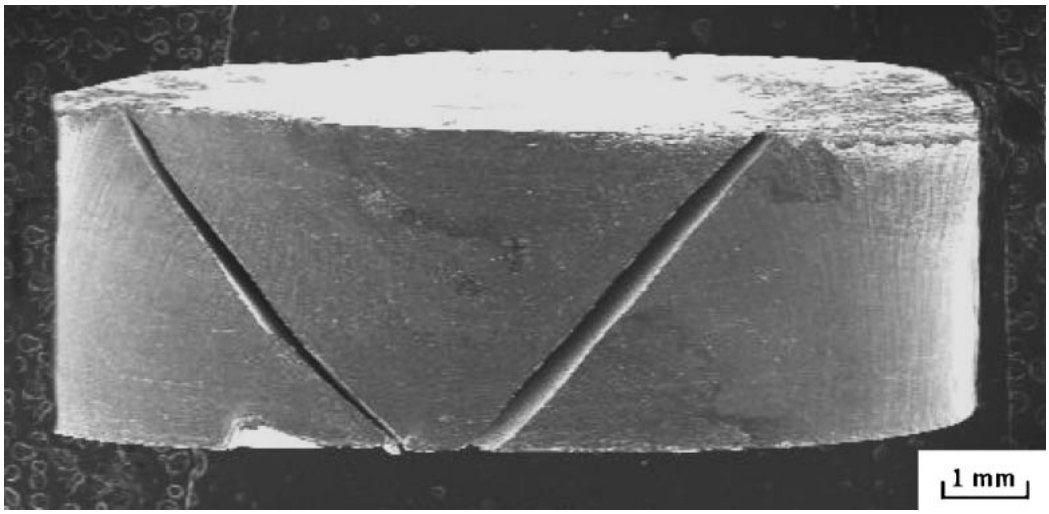

(a)

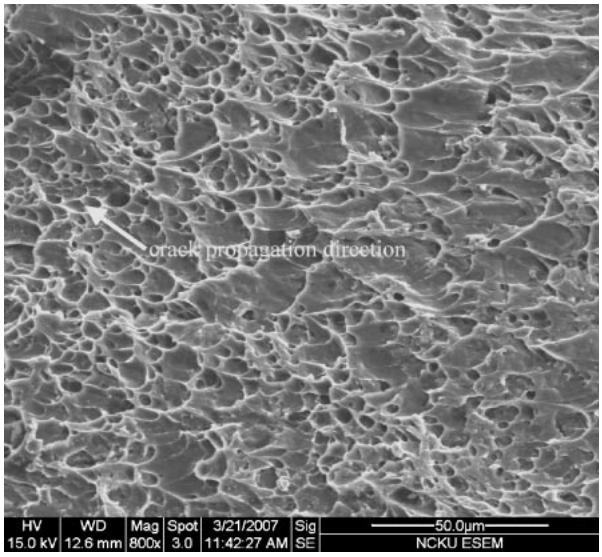

(b)

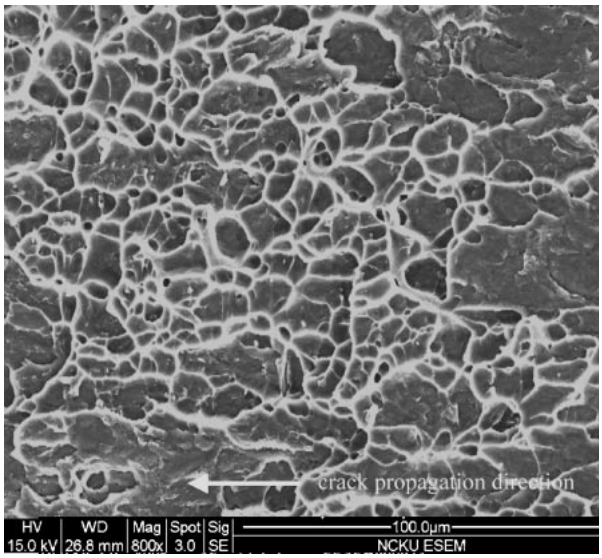

(c)

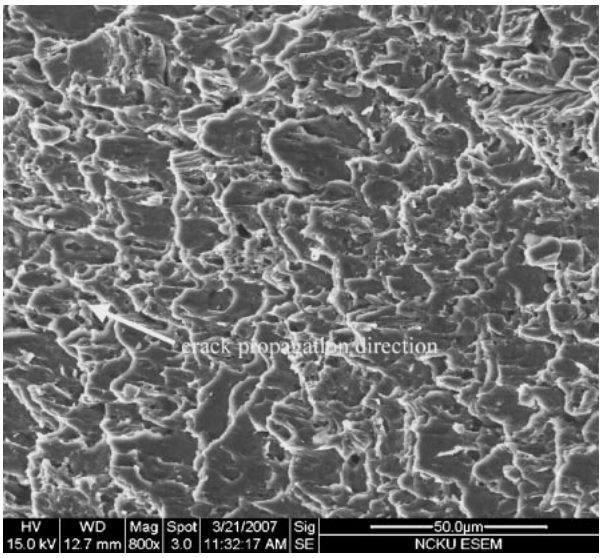

(d)

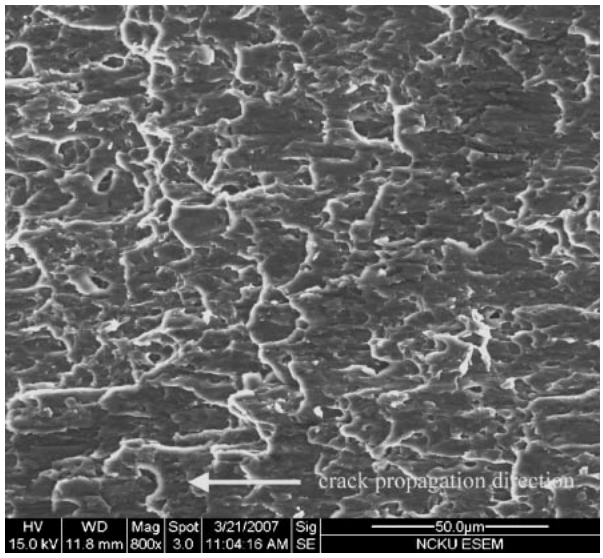

(e)

Fig. 6 (a) Low-magnification SEM fractograph of specimen deformed at strain rate of $3.6 \times 10^3\ s^{-1}$. Scanning electron micrographs showing fracture surfaces of specimens deformed at strain rates of: (b) $2.2 \times 10^3\ s^{-1}$, (c) $3.6 \times 10^3\ s^{-1}$, (d) $4.7 \times 10^3\ s^{-1}$, and (e) $5.9 \times 10^3\ s^{-1}$.

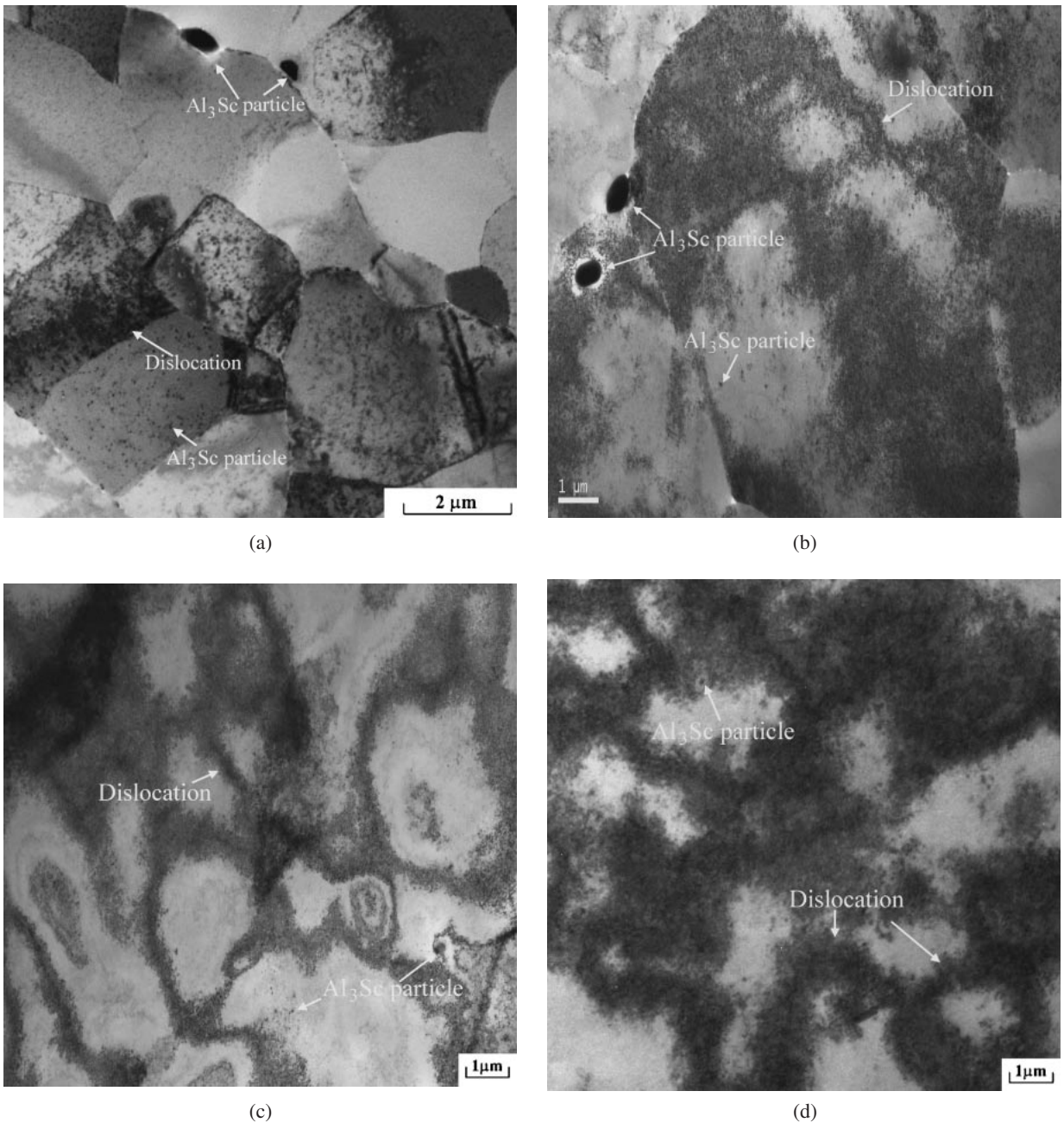

Fig. 7 (a) Transmission electron micrograph of undeformed Al-Sc alloy. Dislocation structures of Al-Sc alloy specimens deformed at strain rates of: (b) $1.3 \times 10^3\ s^{-1}$, (c) $3.6 \times 10^3\ s^{-1}$, and (d) $5.9 \times 10^3\ s^{-1}$.

of n, L and t were determined by drawing five lines with a total length of L in random directions on TEM images with a magnification of 100000×, and then counting the total number of dislocations intersecting these lines in order to obtain the value of n. Finally, the foil thickness, t, was measured using a convergent beam diffraction technique. Figure 8(a) shows the variation of the reciprocal of the cell size with the dislocation density as a function of the strain rate. It is observed that an increasing strain rate increases the dislocation density, but decreases the dislocation cell size. Furthermore, it is found that the dislocation density increases linearly with an increasing strain rate. The higher dislocation density prompts a reduction in the dislocation cell size. Figure 8(b) illustrates the variation of the strain rate sensitivity and the activation volume with the dislocation cell size. It can be seen that a smaller cell size is associated with a higher strain rate sensitivity but a lower activation volume. Figure 8(c) shows that the flow stress increases with a decreasing dislocation cell size as a consequence of the higher dislocation density. The higher flow stress is indicative of a higher work hardening rate and results in a lower value of the dislocation cell size to cell wall thickness ratio.

4. Conclusion

Utilising a compressive SHPB system, this study has examined the dynamic deformation behaviour, fracture characteristics and microstructural evolution of high-strength weldable Al-Sc alloy at strain rates ranging from $1.3 \times 10^3\ s^{-1}$ to $5.9 \times 10^3\ s^{-1}$ under room temperature

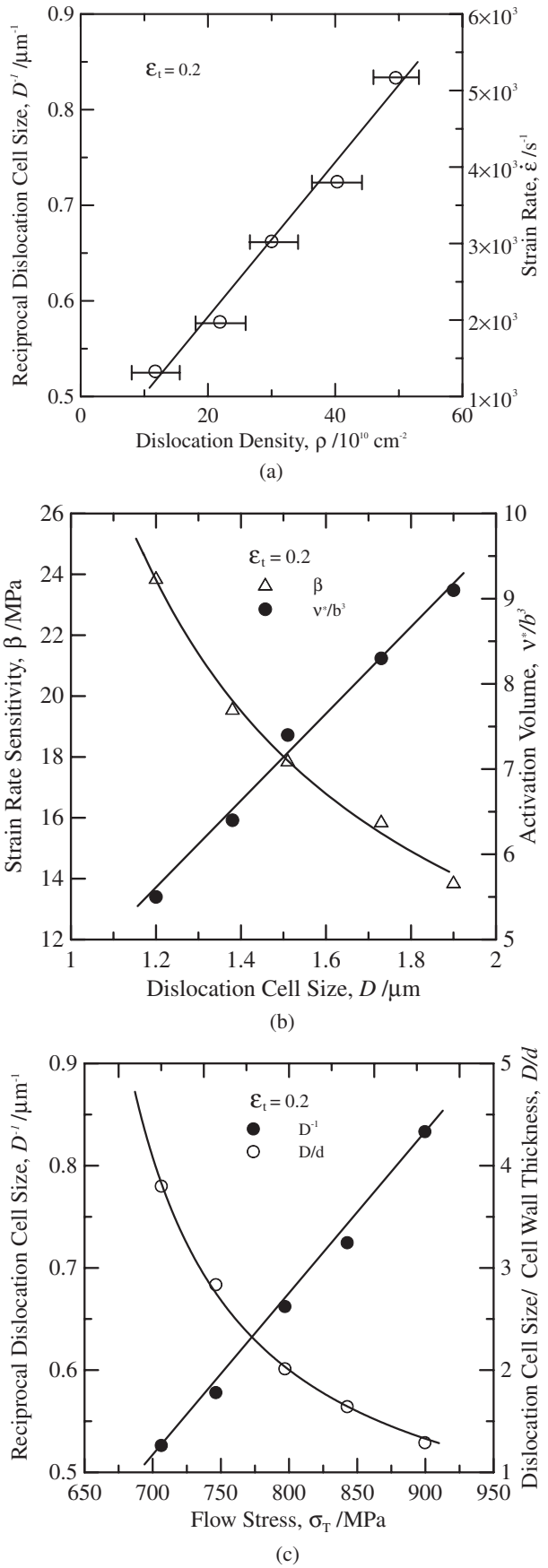

Fig. 8 (a) Variation of reciprocal of dislocation cell size with dislocation density as function of strain rate at fixed strain of 0.2; (b) variation of strain rate sensitivity and activation volume with dislocation cell size; and (c) variation of reciprocal of dislocation cell size and ratio of dislocation cell size to cell wall thickness with flow stress.

conditions. The results have shown that the flow stress of the Al-Sc alloy increases with an increasing strain rate. The work hardening rate also increases with increasing strain rate, but decreases with increasing strain as a result of limited dislocation motion within the microstructure. The results have also revealed that the strain rate sensitivity increases but the activation volume decreases with an increasing work hardening stress. A good agreement has been observed between the experimental results for the stress-strain response of the current Al-Sc alloy and those predicted using the Zerilli-Armstrong FCC constitutive law. SEM observations have revealed that the weldable Al-Sc specimens fracture as a result of a localised shear effect. The fracture surfaces are characterised by a transgranular dimple-like structure, which indicates a ductile failure mode. Both the depth and the density of the dimples decrease as the strain rate increases. The TEM microstructural observations have shown that the dislocation density increases with an increasing strain rate. It has been shown that the higher values of flow stress observed at high strain rates can be attributed to a rapid generation and accumulation of dislocations within the microstructure as a result of the resistance to dislocation motion posed by the Al_3Sc precipitates within the matrix and at the grain boundaries. The rapid generation of dislocations at higher strain rates results in a significant increase in the dislocation density and therefore prompts a notable improvement in the flow strength of the Al-Sc alloy. Furthermore, the high degree of interaction between the dislocations and the precipitates at higher strain rates leads to an increased work hardening effect.

Acknowledgment

The authors gratefully acknowledge the financial support provided to this study by the National Science Council (NSC) of Taiwan under Contract No. NSC 95-2221-E-006-270. The authors also with to express their appreciation to Taiwan Hodaka Technology Co. Ltd. for their supply of Al-Sc alloy bars.

REFERENCES

1) L. S. Kramer, W. T. Tack and M. T. Fernandes: Adv. Mater. Process. **152** (1997) 23–24.
2) L. M. Dougherty, I. M. Robertson and J. S. Vetrano: Acta Mater. **51** (2003) 4367–4378.
3) M. J. Jones and F. I. Humphreys: Acta Mater. **51** (2003) 2149–2159.
4) V. Ocenasek and M. Slamova: Mater. Charact. **47** (2001) 157–162.
5) V. Jindal, P. K. De and K. Venkateswarlu: Mater. Lett. **60** (2006) 3372–3375.
6) N. A. Belov, A. N. Alabin, D. G. Eskin and V. V. Istomin-Kastrovskii: J. Mater. Sci. **42** (2006) 5890–5899.
7) T. Torma, C. E. Kovács, T. Turmezey, T. Ungár and I. Kovács: J. Mater. Sci. **24** (1989) 3924–3927.
8) F. Musin, R. Kaibyshev, Y. Motohashi and G. Itoh: Scr. Mater. **50** (2004) 511–516.
9) H. Akamatsu, T. Fujinami, Z. Horita and T. G. Langdon: Scr. Mater. **44** (2001) 759–764.
10) S. Lee, A. Utsunomiya, H. Akamatsu, K. Neishi, M. Furukawa, Z. Horita and T. G. Langdon: Acta Mater. **50** (2002) 553–564.
11) B. Irving: Weld. J. **11** (1997) 53–57.
12) C. S. Paglia, K. V. Jata and R. G. Buchheit: Mater. Sci. Eng. A **424** (2006) 196–204.

13) I. N. Fridlyander, A. V. Dobromyslov, E. A. Tkachenko and O. G. Senatorova: Met. Sci. Heat Treat. **47** (2005) 269–275.
14) O. N. Senkov, R. B. Bhat, S. V. Senkov and J. D. Schloz: Metall. Mater. Trans. A **36A** (2005) 2115–2126.
15) W. S. Lee, W. C. Sue, C. F. Lin and C. J. Wu: J. Mater. Process. Tech. **100** (2000) 116–122.
16) W. S. Lee, J. C. Shyu and S. T. Chiou: Scr. Mater. **41** (2000) 51–56.
17) H. Conrad: J. Metal. **16** (1964) 582–588.
18) A. Cuniberti and A. Picasso: Phys. Stat. Sol. (a) **183** (2001) 373–379.
19) L. Shi and D. O. Northwood: Acta Metall. Mater. **43** (1995) 453–460.
20) H. Kobayashi and B. Dood: Int. J. Impact Eng. **8** (1989) 1–13.
21) G. R. Johnson and W. H. Cook: *Pro. 7th International Symposium on ballistics* (The Netherland, 1983) pp. 541–547.
22) F. J. Zerilli and R. W. Armstrong: J. Appl. Phys. **61** (1987) 1816–1825.
23) F. J. Zerilli and R. W. Armstrong: Acta Metall. Mater. **40** (1992) 1803–1808.
24) L. E. Murr: *Shock Wave and High-Strain Rate Phenomena in Metals: Concept and applications* (New York: Plenum Press, 1981) pp. 607–73.
25) R. K. Ham: Phil. Mag. **6** (1961) 1183–1184.